

# Empirical millimeter-wave wideband propagation characteristics of high-speed train environments

Jae-Joon Park  | Juyul Lee  | Kyung-Won Kim  | Heon-Kook Kwon | Myung-Don Kim

Telecommunications and Media  
Research Laboratory, Electronics and  
Telecommunications Research Institute  
(ETRI), Daejeon, Rep. of Korea

## Correspondence

Jae-Joon Park, Telecommunications and  
Media Research Laboratory, Electronics  
and Telecommunications Research Institute  
(ETRI), Daejeon, Rep. of Korea.  
Email: jjpark@etri.re.kr

Owing to the difficulties associated with conducting millimeter-wave (mmWave) field measurements, especially in high-speed train (HST) environments, most propagation channels for mmWave HST have been studied using methods based on simulation rather than measurement. In this study, considering a linear cell layout in which base stations are installed along a railway, measurements were performed at 28 GHz with a speed up to 170 km/h in two prevalent HST scenarios: viaduct and tunnel scenarios. By observing the channel impulse responses, we could identify single- and double-bounced multipath components (MPCs) caused by railway static structures such as overhead line equipment. These MPCs affect the delay spread and Doppler characteristics significantly. Moreover, we observed distinct path loss behaviors for the two scenarios, although both are considered line-of-sight (LoS) scenarios. In the tunnel scenario, the path loss exponent (PLE) is 1.3 owing to the waveguide effect, which indicates that the path loss is almost constant with respect to distance. However, the LoS PLE in the viaduct scenario is 2.46, which is slightly higher than the free-space loss.

## KEYWORDS

Doppler, high-speed train, millimeter-wave, path loss, propagation measurement

## 1 | INTRODUCTION

During the standardization process for developing radio interface specifications of fifth generation (5G) mobile communication systems, known as International Mobile Telecommunications-2020 (IMT-2020), the ITU-R has been evaluating the proposed candidate technologies [1]. 5G is anticipated to maintain high-quality services at a high mobility up to 500 km/h, which is envisioned particularly for high-speed trains (HSTs). To provide guidelines for the evaluation,

the ITU-R published a new report in 2017 [2], which includes a linear cell layout for millimeter-wave (mmWave) HSTs, in which the base stations are placed along the rail track. Although the report provides evaluation channel models to consider a wide range of scenarios such as indoor, urban, and rural areas, it does not include HST scenarios. Furthermore, existing channel models rarely support mmWave HST scenarios [2,3]. Notably, the WINNER II channel model [4] can provide a moving network scenario for HST in a rural area below a frequency of 6 GHz, but not above 6 GHz. In this

study, we experimentally investigate the channel characteristics of HST environments in the mmWave band.

We performed measurement campaigns in a linear cell layout for HSTs at the 28 GHz band, which is one of the 5G frequency bands defined by 3GPP [5]. Generally, HST propagation scenarios can be classified as follows: open space, viaduct, cutting, hilly terrain, tunnels, and stations [6]. Our measurement campaigns were conducted in two of the aforementioned scenarios: viaduct and tunnel scenarios. Due to the difficulties (mainly safety issues) involved in performing experiments at a commercial high-speed railway, we conducted the measurements on a test track constructed solely for evaluation purposes. We considered a linear cell layout in which a transmitter (TX) is positioned along a railway track and a receiver (RX) is installed on the roof of a train carriage. A test HST was used as the RX, and we were allowed to install an antenna on its roof. During the measurements, the RX was moved at a speed of up to 170 km/h, and there were no other moving vehicles around the RX.

Accurate propagation characteristics need to be known for system development and performance evaluation. Numerous studies have been conducted on sub-6-GHz HST propagation measurements [7–10]. In [7], measurements were conducted at 930 MHz with a speed up to 350 km/h along a high-speed railway to propose a hybrid path loss model for viaduct and cutting scenarios. Zhou and others [8] performed channel measurements at 1.89 GHz in an open-type train station environment along a high-speed railway with an average velocity of 285 km/h in China. Large- and small-scale characteristics, such as path loss, shadow fading, Ricean K-factor, and delay spread, were investigated and modeled. Domínguez-Bolaño and others [9] experimentally investigated propagation characteristics such as path loss, power delay profile, delay spread, and Doppler power spectral density based on the measurements of the HST channel at 2.6 GHz in a rural area in Spain.

Thus far, mmWave propagation characteristics have been intensively investigated for typical scenarios, such as urban micro-/macro-cell and indoor scenarios [11–14]. Several studies on measurement-based mmWave HST have been reported [15–17]. Among these, [15] conducted propagation measurements in a subway line at 31 GHz with a bandwidth of 250 MHz and in a ray-tracing (RT) simulator calibrated and validated using the measurement. Through intensive RT simulations, mmWave HST propagation characteristics such as path loss, Doppler shifts, and coherence time were demonstrated for various HST scenarios such as urban, rural, and tunnel scenarios. However, the RX antenna was installed inside a subway and the measurements were mainly used for the calibration and validation of the RT simulations.

Kim and others [16] investigated the measurement and modeling of a 28 GHz HST mobile wireless backhaul channel in a rural scenario. The measurements were conducted at a freight depot with several train tracks, trees, and buildings. However, pickup trucks were used as measurement vehicles instead of a train. This may limit the effects of the body of the train on the propagation. Moreover, the RX was moved along a path next to the train tracks at a constant speed of 6.3 km/h, which is not a realistic train speed. In [17], a measurement campaign was conducted with a 41 GHz mmWave system dedicated to HST communications in a 2-km-long straight section, which is not an HST but a street-level environment. The measurement was conducted at the relative speed between the TX and RX of 170 km/h, to investigate the propagation characteristics for a moving HST. As in [16], both the TX and RX antennas were placed on top of two vehicles at a height of 2 m above the ground. Due to the difficulty involved in conducting channel measurement in mmWave HST environments, the mmWave channel characteristics in various HST scenarios have been investigated mostly through RT simulations [18,19].

To sum up, most HST propagation papers have focused on characteristics below 6 GHz. Although there are few papers on HST propagation concerning mmWave frequency bands, these papers do not sufficiently cover various HST environments. Consequently, the deployment of mmWave wireless systems in HST environments could be limited. To fill this gap, in this study, we conducted field measurements in an HST environment at the 28 GHz band. Furthermore, based on the measurements in two HST scenarios, we investigated the propagation characteristics for each scenario and the evolution of the propagation characteristics during a transition between scenarios, for example, from a viaduct to a tunnel scenario or vice versa. In addition, the effects of railway structures unique to HST environments on the channel characteristics were investigated.

## 2 | MEASUREMENT CAMPAIGN

As mentioned earlier, the literature on mmWave HST propagation measurements is limited. Commercial HSTs are being operated in several countries, such as Korea, Japan, China, and France. However, there are no mmWave wireless communication systems between base stations and HSTs. Performing measurements at the mmWave band in an HST environment is still challenging.

Thanks to the support from the Korea Railroad Research Institute (KRII), we could conduct wideband mmWave propagation measurements with an actual HST on a dedicated railway track. All the safety issues were dealt with before conducting the measurements.

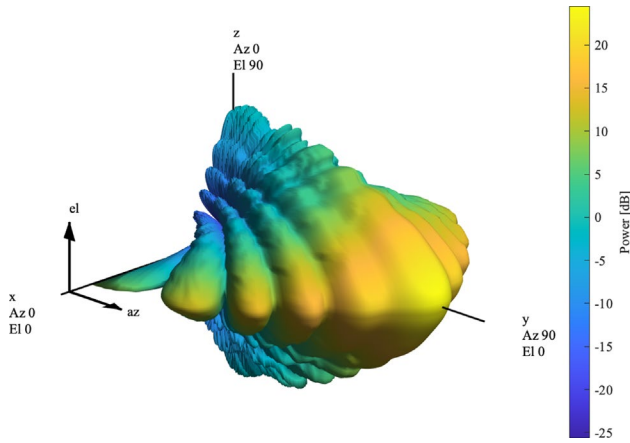


**FIGURE 1** Radiation pattern of the TX directional horn antenna

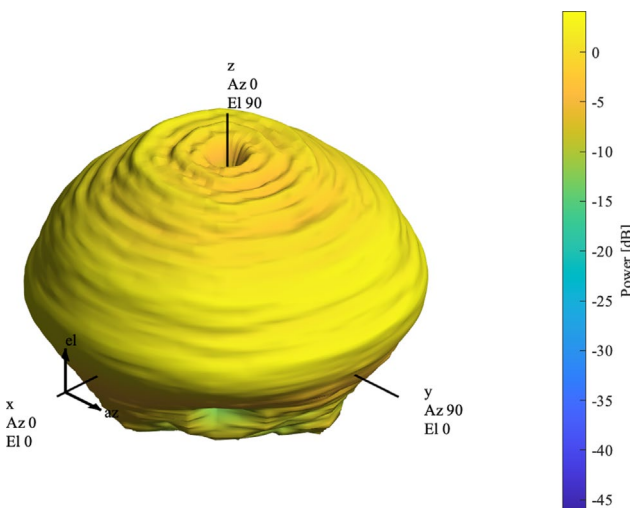


**FIGURE 2** Radiation pattern of the RX omnidirectional antenna

**TABLE 1** Channel sounder specifications

Parameters	Values
Center frequency [GHz]	28
Channel bandwidth [MHz]	500
Probing signal (PN sequence) length [chips]	4095
Multipath resolution [ns]	2
Maximum TX power (w/o antenna) [dBm]	29
TX antenna (10° HPBW) gain [dBi]	23.2
RX antenna (omnidirectional) gain [dBi]	3.2

## 2.1 | Channel sounder

We conducted HST measurements using a wideband band exploration and channel sounder (BECS) developed by Electronics and Telecommunications Research Institute

(ETRI) in the Rep. of Korea [13,20]. The sounder uses a pulse compression technique based on the periodic transmission of a probing signal in the time domain [21]. The sounder comprises a baseband module, transceiver module, timing module (TIM), and RF up-/down-converter module (RFM).

For the TX, we used a directional horn antenna with a half-power beamwidth (HPBW) of 10°. Figure 1 shows the radiation pattern of the TX antenna. The TX antenna periodically transmits a probing signal to the RX. The probing signal is designed to be identified at the RX using the cross correlation property. We used a pseudo-noise (PN) sequence as the probing signal. The TX and RX can be synchronized in remote channel sounding operations by using rubidium oscillators in the TIM.

The RX uses a monopole-type omnidirectional antenna, as shown in Figure 2, which is intended to capture multipath components (MPCs) from all directions. The center frequency and maximum channel bandwidth of the sounder are 28 GHz and 500 MHz, respectively. The sounder utilizes complex-valued channel impulse responses (CIRs) to investigate the propagation characteristics such as path loss, delay spread, Ricean K-factor, and Doppler shift. In particular, a PN sequence with a length of 4095 is periodically transmitted from the TX to the RX while maintaining synchronization between them. With some system and propagation delays, the transmitted signal and its multipath replica arrive at the RX. The detailed sounder specifications are listed in Table 1.

## 2.2 | Measurement scenario and setup

A measurement campaign was conducted on a comprehensive railway test track located in Osong, Korea. Owned by the Korean government and operated by the KRRI, the 13-km track is comprised of high-speed sections (speeding up to 230 km/h), sharp curves, slopes, nine bridges, and six tunnels for performance tests. In the high-speed sections, the railway track is installed in a long straight line to speed up a train. Figure 3 shows the overall measurement environment. The measurement was conducted in a high-speed section for a distance range of 1216 m. This range consists of three sections categorized into two different propagation scenarios: viaduct scenario (Segments A and C) and tunnel scenario (Segment B). As shown in Figure 4, the distance between the TX and the entrance to Tunnel #4, which is Segment A, is approximately 179 m and the length of Tunnel #4, which is Segment B, is 271 m. During the measurements, the height of the TX antenna is slightly greater than that of the RX antenna, and a line-of-sight (LoS) link can be established between the TX and RX in all the segments. In addition, the distance between the exit from Tunnel #4 and the entrance to Tunnel #5, which is Segment C, is 766 m. The details are summarized in Table 2.

The train used in the measurement is the so-called “HEMU” (HEMU stands for high-speed electric multiple

unit), provided by the KRRI, as shown in Figure 3. It was designed to travel at a maximum speed of 430 km/h. At the time of our measurement campaign, the train was being simultaneously utilized in other testing activities for high-speed operation. The dimensions of the HEMU are 150 m × 3.1 m × 3.75 m (Length × Width × Height) including six cars. The first and last cars of the train have two electric locomotives so that the train can move in both directions without a U-turn. For safety reasons, the maximum speed of the train was limited to 170 km/h during the measurement campaign.

The measurement was performed 14 times (“one time” indicates to perform a measurement while the RX is moving from the TX to Tunnel #5, or vice versa): 6 times in the direction from Tunnel #3 to Tunnel #4 (the receiving antenna was located at the first car in the moving direction), and 8 times in

the opposite direction (the receiving antenna was located at the last car in the moving direction; see Table 3).

There were steel structures including overhead line equipment (OLE) along the test track to provide high-voltage electricity to the train (see Figures 3 and 4). As shown in Figure 6, there were pantographs on the roof of the test train, which can receive the electric power. Notably, there were no other moving objects during the measurement campaign. We placed the TX RFM and antenna next to the test track at a height of 5 m, as shown in Figure 5. We utilized a custom-built sturdy antenna master to endure the windblast from the HST. The other parts of the TX channel sounder were located inside a vehicle (white dashed line in the left part of Figure 5). The RFM and RX antenna were installed on the roof of the train carriage, and the other parts were placed inside the train carriage, as shown in



FIGURE 3 Overall measurement environment (left) and HEMU high-speed train (right)

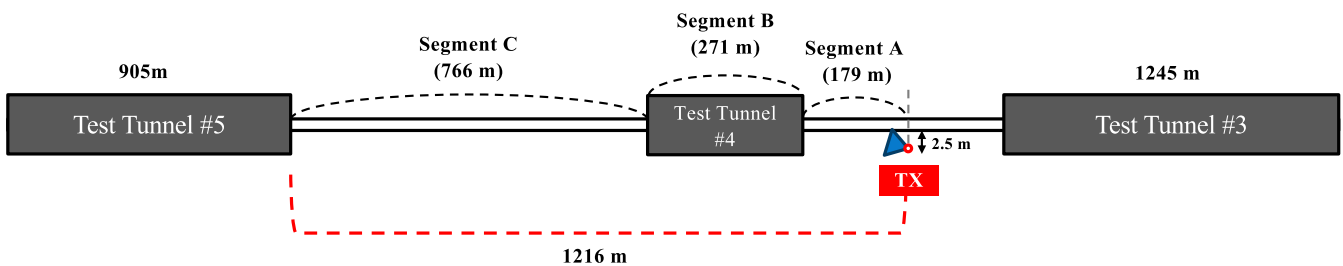


FIGURE 4 Sketch of the overall measurement campaign

TABLE 2 Propagation scenario for each section

	Propagation scenario	Length [m]
Segment A	Viaduct	179
Segment B	Tunnel	271
Segment C	Viaduct	766

TABLE 3 Train runs for measurements

RX moving direction	Number of train runs
Test tunnel #3 → #4	6
Test tunnel #4 → #3	8
Total	14

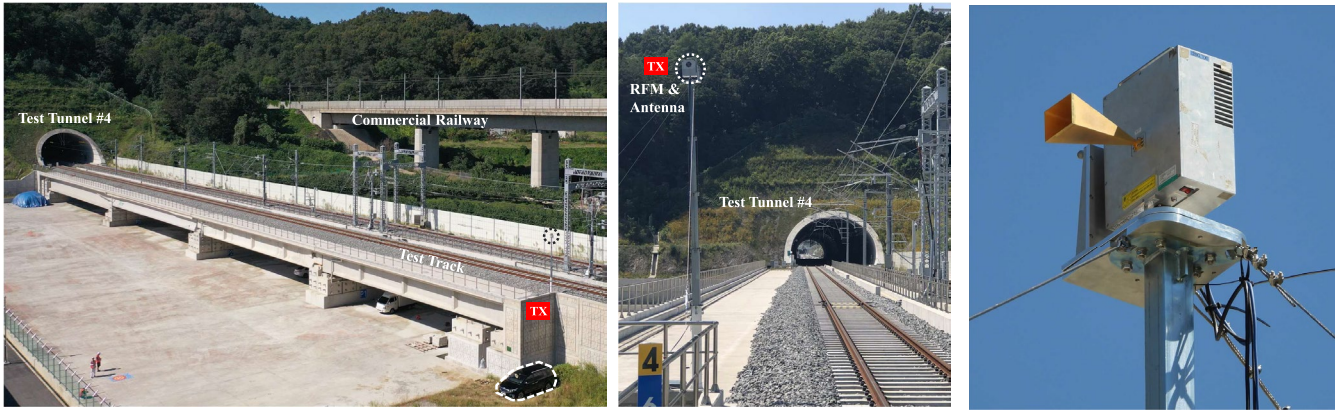


FIGURE 5 TX channel sounder setup (left and middle) and TX RFM & antenna (right)

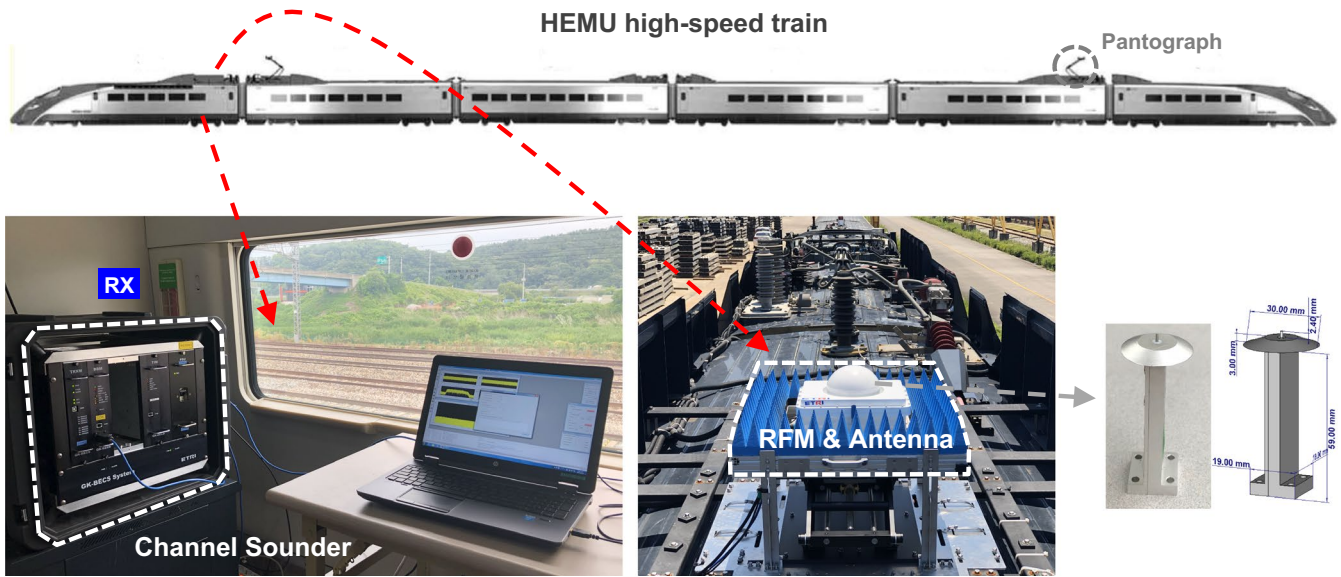


FIGURE 6 RX channel sounder setup and RX antenna

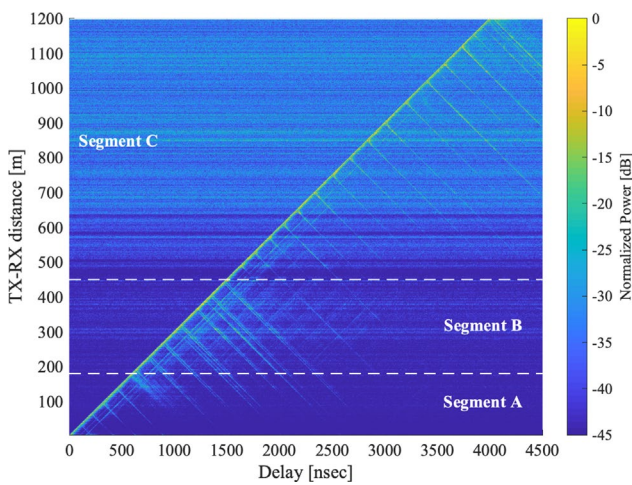


FIGURE 7 Exemplary concatenated PDPs in the HST measurements

Figure 6. The height of the RX antenna was 4.2 m above the ground.

As the train moves at high speeds, we conducted the measurement campaigns carefully to prevent accidents. We installed the RX RFM and antenna tightly onto the train roof by using a jig (see Figure 6). We also mounted a Radome upon the antenna to reduce the effects of wind on the moving HST. Moreover, we attached absorbers around the RX RFM and antenna to mitigate the influence of reflected multipaths from the jig.

### 3 | DATA ANALYSIS RESULTS

#### 3.1 | Power delay profiles

A power delay profile (PDP) provides the intensity of a signal received through a multipath channel as a function of time delay.

Figure 7 illustrates exemplary concatenated PDPs for the entire distance range of the measurement. In the figure, the horizontal axis, vertical axis, and color code denote the propagation delay, TX-RX distance (the distance can be calculated using time and the speed of 42 m/s), and normalized received power in dB, respectively. The white dashed lines, at approximately 180 m and 450 m, indicate the locations of the entrance and exit of Tunnel #4, respectively. We depict an enlarged version of Segment A as shown in Figure 8, to investigate the multipath characteristics of the HST propagation channel in detail. Furthermore, Figure 9 shows a simplified layout of Segment A. It describes the locations of scatters, which are OLEs regularly installed next to the test track.

It can be observed from Figures 7 and 8 that there are multiple trajectories in the distance-delay domain. From the figures, we can observe that:

- a. The LoS propagation trajectory can be observed in both figures.
- b. There are several trajectories starting regularly from the LoS trajectory, which are indicated by circled numbers, ①, ②, ③, and ④, in Figure 8. These are single-bounced MPCs associated with the OLE along the test track depicted in Figure 9. For example, as the RX approaches an OLE, the propagation delay of a single-bounced MPC from the OLE is decreased. After the RX passes the OLE, the difference in propagation delay between the single-bounced

- MPC and the LoS path is not large, and it is shown as the LoS trajectory.
- c. There are several parallel trajectories to the LoS trajectory. This is due to the double-bounced MPCs from the scatters. For example, a parallel trajectory can be generated from a multipath bounced on scatterer ② and then scatterer ①. After the RX passes the scatters, a double-bounced MPC has a fixed delay compared with the LoS path.
- d. Before entering Tunnel #4, indicated by the white dashed line at 180 m, there are multipaths in a distance range of 120 m to 180 m and a delay range of 600 ns to 800 ns. They are generated from a concrete structure around the entrance of the tunnel (see Figure 5).
- e. Owing to the waveguide effect in a tunnel, in addition to the MPCs from the OLEs, there are more multipaths in Segment B than in the others.

Regarding property (a), we can find a similar observation in [9], in which the measurements were conducted in a rural area at sub-6-GHz bands. However, property (c) is unique to this study.

### 3.2 | Path loss

The path loss (PL) is the ratio between the transmitting and receiving powers. This is an important propagation characteristic for system planning and coverage/interference analysis. We analyzed the measurement data to fit the alpha-beta (AB) model [12], which is given by

$$PL_{AB}(d) = 10\alpha \log_{10}(d) + \beta + X_{\sigma}, \quad (1)$$

where  $d$  is the distance from TX to RX,  $\alpha$  is the slope,  $\beta$  is the floating offset value, and  $X_{\sigma}$  is the log-normal shadow fading factor parameterized by the shadow fading standard deviation  $\sigma$ . By fitting our measurement data to (1), we obtain the parameters  $\alpha$  and  $\beta$ . In the fitting, we subsampled all the measurement data at every 1 m by calculating the local median. The standard deviation  $\sigma$  of the shadowing is calculated using the standard deviation of the difference between the measured PL and the fitting model.

Figure 10 shows the measured PL result and the result from the fitted AB model. Note that only the effective

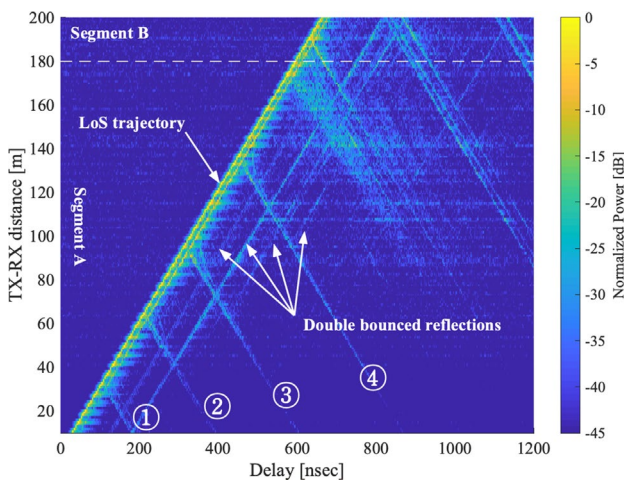


FIGURE 8 Enlarged PDPs of segment A

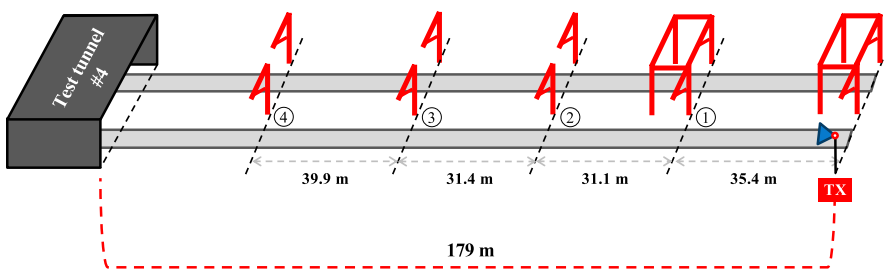


FIGURE 9 Simplified layout of segment A

measurement data between 40 m and 900 m are used for the analysis due to the high directivity of the transmit antenna [9]. In the figure, the dashed lines at approximately 180 m and 450 m indicate the locations of the tunnel entrance and exit, respectively. As the measured PL has significantly different patterns in Segments A, B, and C, we estimate  $\alpha$  and  $\beta$  separately in each segment, as summarized in Table 4. To evaluate our measurement modeling results, we summarize the path loss exponent (PLE) and shadowing statistics from the literature in Table 5.

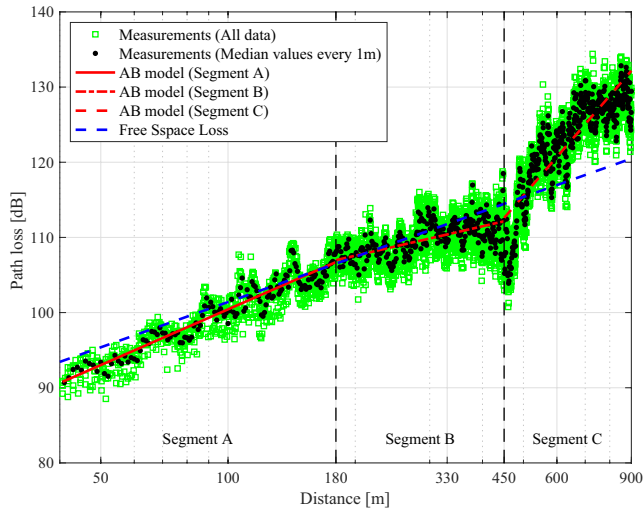


FIGURE 10 Path loss and least-squares fitting results

TABLE 4 Estimated path loss parameters

	$\alpha$	$\beta$	$\sigma$ [dB]
Segment A	2.46	51.2	1.4
Segment B	1.30	77.7	1.8
Segment C	6.51	-60.0	3.0

TABLE 5 Summary of path loss exponent and shadow fading in similar HST scenarios at various frequencies

Scenario	Frequency [GHz]	PL exponent ( $\alpha$ )	SF std. [dB]	Antenna type	Ref.
Tunnel (straight)	28	1.30	1.8	TX: directional (10° HPBW)	This work
Viaduct		2.46	1.4	RX: omnidirectional	
Rural	28	2.27	2.8	TX: omnidirectional RX: virtual circular array	[16,22]
Viaduct	2.35	3.03	2	TX: omnidirectional RX: omnidirectional	[23]
Tunnel (straight)	2.45	1.58	5.9	TX: omnidirectional	[24]
	5.7	1.62	4.4	RX: omnidirectional	
Tunnel (curved)	2.4	5.37	4.67	TX: panel antenna (75° HPBW)	[25]
	5.705	4.94	4.46	RX: Log-Periodic antenna (85° HPBW)	
Tunnel (straight)	31.625	1.43	6.2	TX: directional (20° HPBW)	[15] <sup>a</sup>
Tunnel (curved)		4.4	10.9	RX: directional (8° HPBW)	

<sup>a</sup>Ray-tracing (RT) simulation results.

As described in the previous section, Segments A and C represent the viaduct scenario and Segment B represents the tunnel scenario. Even though Segment A has an LoS link, the PLE is 2.46, which is slightly higher than that of the free-space model. We believe that this is due to the reflections from a concrete structure around the tunnel entrance, the similar antenna heights of the TX and RX, and the effect of the train carriage roof. Although it is not the same environment, this value is between 2.27 and 3.03, which are the PLE values of a rural scenario at 28 GHz and a viaduct at 2.35 GHz, respectively, as shown in Table 5. This implies that the PLE can differ depending on the frequency and measurement setup, even in the same environment, such as a viaduct.

The PLE of Segment B is 1.30, which indicates that the PL is almost constant with respect to distance. This value is consistent with the literature, as shown in Table 5. For instance, the PLE in [15] is 1.43, which proposed a directional PL model based on an RT simulation in a straight tunnel scenario. It can be observed that the PL increases with respect to distance up to 330 m and subsequently remains constant. This appears to be due to the waveguide effect in the tunnel. Furthermore, it can be observed from Table 5 that straight tunnels have smaller PLEs than curved ones. In Segment C, the path loss exponent is 6.51. We can observe that the PL increases rapidly immediately after the tunnel exit. This can be explained by the fact that the transmitted signal is blocked by the HST because the receiving antenna is located on the first or last car, depending on the direction of movement. Furthermore, the signals reflected from the tunnel can be scattered in various directions immediately after the tunnel exit. Thus, the received power can suddenly decrease, resulting in a high PLE value.

Figure 11 shows the estimated cumulative probabilities of  $X_\sigma$  along with the theoretical Gaussian cumulative distribution functions (CDFs). It is observed that the measured SF and the Gaussian CDF fit are consistent with each other.

### 3.3 | Delay spread

The root-mean-square (RMS) delay spread is an important parameter characterizing the temporal dispersive properties of multipath channels. From the measurement data, we obtained the RMS delay spread values for each segment. The RMS delay spread ( $\sigma_{DS}$ ) was calculated from the measured PDPs as follows:

$$\sigma_{DS} = \sqrt{\frac{\sum_{l=1}^L (\tau_l - \bar{\tau})^2 \cdot P_l}{\sum_{l=1}^L P_l}}, \quad (2)$$

where  $\tau_l$  and  $P_l$  denote the delay and power of the  $l$ -th multipath, respectively, where  $l \in [1, \dots, L]$  with  $L$  representing the total number of multipaths. Moreover, the average delay ( $\bar{\tau}$ ) is given by

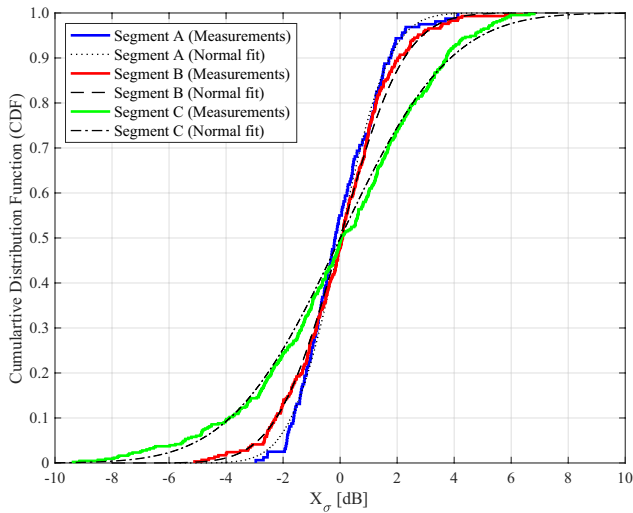


FIGURE 11 Estimated cumulative probabilities of shadow fading

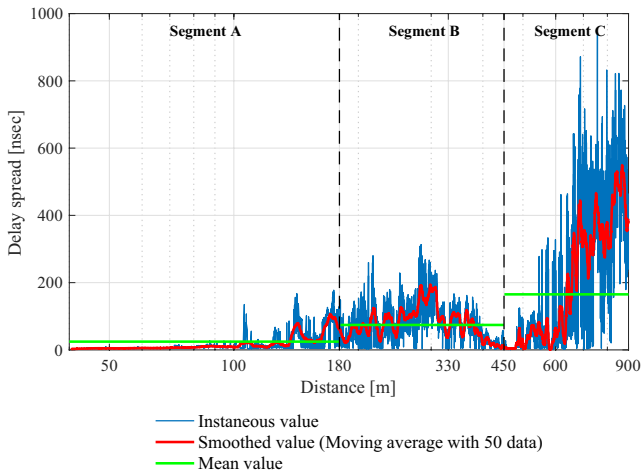


FIGURE 12 Estimated RMS delay spread for all the segments

$$\bar{\tau} = \frac{\sum_{l=1}^L \tau_l \cdot P_l}{\sum_{l=1}^L P_l}. \quad (3)$$

The threshold was set to 20 dB from the peak component in each PDP to determine the effective multipath components. Figure 12 illustrates the estimated RMS delay spread for all the segments. A curve corresponding to the smoothed values by means of the moving average with a window size of 50 is included, in addition to the mean delay spread for each segment.

From Figure 12, we can observe the following characteristics:

- The delay spread in Segment A, which represents the viaduct scenario, is mostly small. However, in a distance range of 120 m to 180 m, the delay spread relatively increases due to the MPCs from a concrete structure around the entrance of Tunnel #4. This result is consistent with the PDP characteristics in the same segment.
- In the tunnel environment (Segment B), the greatest delay spread values were observed at the middle of the tunnel and the delay spread becomes small at the end of the tunnel. This is because the waveguide effect can be

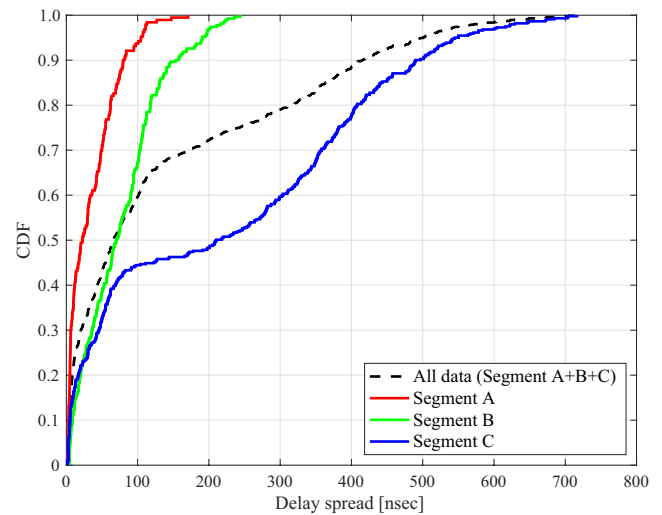


FIGURE 13 Estimated CDFs for each segment

TABLE 6 Typical RMS delay spread values

	RMS delay spread [nsec]		
	10%	50%	90%
Segment A	3.3	22.4	79.6
Segment B	8.3	70.4	152.9
Segment C	5.1	209.3	489.5
All data	5.2	65.0	414.3

maximized in the middle of the tunnel. In addition, fewer MPCs are received from the outside of the tunnel, as the receiving antenna becomes closer to the tunnel exit.

- c. In segment C, the delay spread is relatively small before the train completely exits the tunnel, which is at approximately 600 m, as the end of Segment B is 450 m and the train length is approximately 150 m. Subsequently, the delay spread rapidly increases.

The resulting CDFs for each segment are shown in Figure 13, and the typical RMS delay spread values of 10%, 50%, and 90% of the cumulative distribution probability are summarized in Table 6. The mean values of the RMS delay spread in HST environments have been reported, for example, 20 ns at a freight depot in a rural environment [16] and 10 ns to 25 ns with a mean of 14.4 ns in a street-level environment [17]. In this work, the mean value of the RMS delay spread is 24.6 ns in the viaduct scenario (Segment A). This result is similar to the aforementioned results. However, our measurements included the transition from a viaduct to a tunnel scenario, and the maximum value in Segment A is larger than that in the literature.

As most cases are LoS, the delay spread values are generally small. However, the characteristics vary greatly depending on the transition of the propagation environment (for example, entrance, middle, and exit of a tunnel environment). As shown in Table 5, in most cases, the delay spread value is 500 ns or less for all the segments.

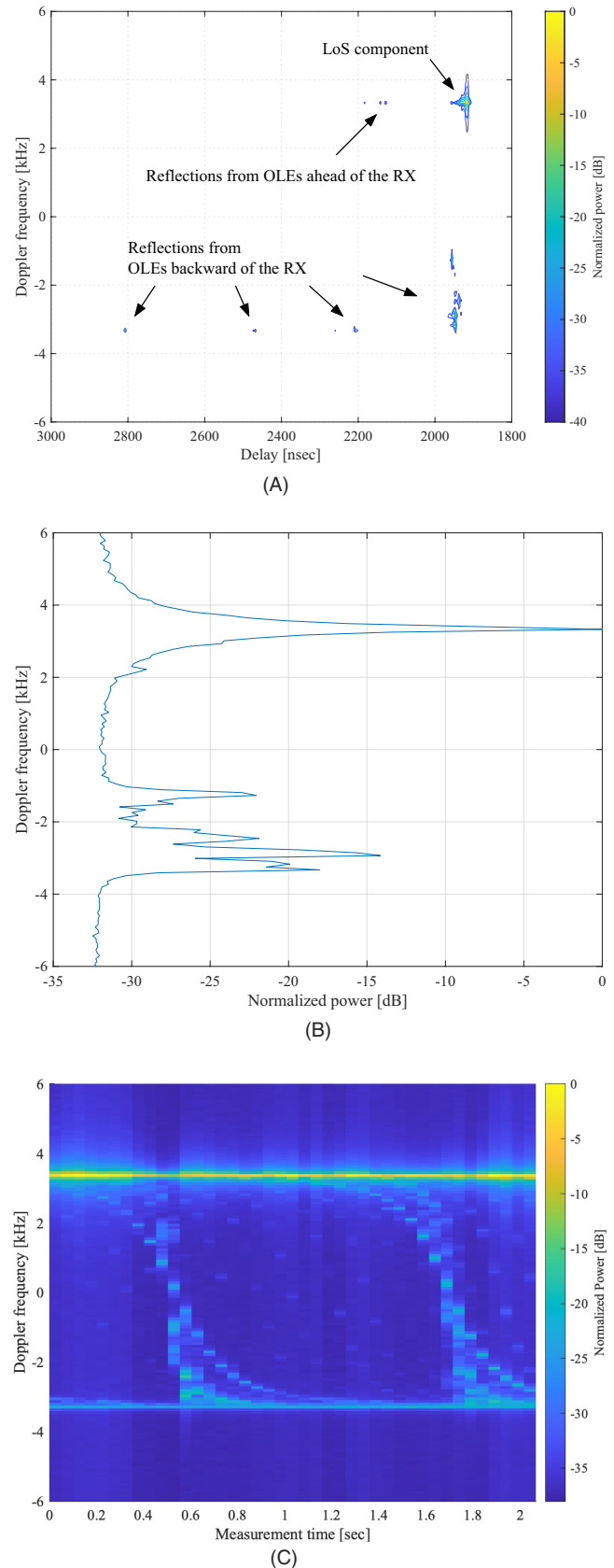
### 3.4 | Doppler shift

Figure 14 depicts an exemplary Doppler spectrum from the HST channel measurement in Segment B. The Doppler shift can be estimated by applying the discrete Fourier transform (DFT) to the measured CIRs with respect to time as follows:

$$h(\nu, \tau) = \text{DFT}\{h(t, \tau)\}_t, \quad (4)$$

where  $t$ ,  $\tau$ , and  $\nu$  denote time, delay, and Doppler shift, respectively. Furthermore,  $h(t, \tau)$  denotes the time-variant CIRs.  $\text{DFT}\{\cdot\}_t$  is the DFT of the input argument with respect to time. The Blackman window is applied prior to the DFT operation to reduce the level of the sidelobes.

A time interval of 385 consecutive CIRs (we called it a cycle, which corresponds to 12.6 ms) was chosen to satisfy the sampling theorem, to estimate the Doppler shift from the measurement. The power delay-Doppler profile (PDDP), in which each delay component is associated with its own Doppler shift, is the magnitude squared value of  $h(\nu, \tau)$ , as shown in Figure 14A. Summing the PDDP over the delay domain yields the Doppler spectrum in Figure 14B. Figure 14C shows the concatenated Doppler spectrum estimated from 42



**FIGURE 14** Exemplary Doppler spectra in segment B: (A) PDDP, (B) Doppler Spectrum, and (C) Concatenated Doppler Spectrum.

cycles. The interval between cycles is 37.8 ms. To summarize, the total measurement duration is approximately 2 s.

Theoretically, the Doppler shift can be expressed as

$$f_D = \frac{f}{c} \times v \times \cos\theta, \quad (5)$$

where  $f$  is the carrier frequency,  $c$  is the speed of light ( $3 \text{ m/s} \times 10^8 \text{ m/s}$ ),  $v$  is the speed of the RX, and  $\theta$  is the angle between the TX and RX. For the Doppler shift estimation, the measurement was performed when the RX was moving toward the TX. From Figure 14, we observed three dominant Doppler shift components.

- a. The first component is an LoS propagation component observed approximately at the positive maximum Doppler shift ( $+|f_{D_{\max}}|$ ), which is +3.3 kHz in the Doppler frequency domain corresponding to the speed of 130 km/h<sup>1</sup> at the carrier frequency of 28 GHz. Furthermore, we can observe MPCs in the delay domain at the same Doppler shift. This component is caused by the double-bounced MPCs created ahead of the RX as described in the PDP characteristics.
- b. The second component exists at approximately -3.3 kHz in the Doppler frequency domain, which is the opposite Doppler frequency to the LoS component. This component is caused by the local scatters, that is, OLE, installed regularly along the test track in the backward direction of the RX. This component is periodically observed in the delay domain as shown in Figure 14A.
- c. Finally, we can observe transitions from  $+|f_{D_{\max}}|$  to  $-|f_{D_{\max}}|$  in Figure 14C, which is the third component. These transitions can occur when the RX passes by the OLE. From (5),  $\theta$  varies from 0 to 180° as the RX passes by the OLE, and the Doppler shift varies from  $+$  to  $-|f_{D_{\max}}|$ . This transition in the Doppler was also reported in [9], which is based on HST measurements at 2.6 GHz in a rural area.

## 4 | CONCLUSION

Utilizing a channel sounder with a bandwidth of 500 MHz at 28 GHz, we conducted propagation measurements in an HST test track. During the measurements, an HST was moving at a maximum speed of 170 km/h. Based on the field measurements, we investigated the propagation characteristics such as path loss, delay spread, and Doppler shift in two HST scenarios. Owing to the waveguide effect, the PLE of the tunnel was observed to be 1.3. However, with the LoS, when there was no waveguide effect, the PLE of the viaduct appeared to be 2.46, which is slightly higher than that of the free-space case. We also observed that railway

structures installed along a track, such as overhead line equipment, considerably affect the propagation characteristics causing single- and double-bounced MPCs. These MPCs affect the delay spread and Doppler characteristics significantly. For example, the mean value of the RMS delay spread is 24.6 ns in the viaduct scenario (Segment A), which is similar to the results of a previous study (20 ns) in a rural environment. However, the maximum value is larger than that in the previous one. We believe that these mmWave HST measurement characteristics will be beneficial in 5G mobile communication systems. One potential direction for future work might be a comparison with ray-tracing techniques [19], which will enable verification of the impact of HST environments by identifying individual MPC behaviors associated with the surrounding objects.

## ACKNOWLEDGMENTS

This work was supported by the Institute for Information & Communications Technology Promotion (IITP) grant funded by the Korean government (MSIT) [2017-0-00066, “Development of time-space based spectrum engineering technologies for the preemptive using of frequency”] [2017-0-01973, “(Korea-Japan) International collaboration of 5G mmWave based Wireless Channel Characteristic and Performance Evaluation in High Mobility Environments”].

## ORCID

Jae-Joon Park  <https://orcid.org/0000-0002-8695-8185>

Juyul Lee  <https://orcid.org/0000-0002-5851-0615>

Kyung-Won Kim  <https://orcid.org/0000-0002-9663-9954>

## REFERENCES

1. Recommendation ITU-R M.2083, *IMT Vision – Framework and overall objectives of the future development of IMT for 2020 and beyond*, 2015.
2. Report ITU-R M.2412, *Guidelines for evaluation of radio interface technologies for IMT-2020*, 2017.
3. 3GPP, *Study on channel model for frequencies from 0.5 to 100 GHz (Release 14)*, Tech. Rep. TR 38.901 v14.0.0, 2017.
4. P. Kyosti et al., *WINNER II channel models*, IST-WINNER II D1.1.2, 2007.
5. 3GPP, *NR; User Equipment (UE) radio transmission and reception; Part 2: Range 2 standalone*, Tech. Rep. TS 38.101-2, 2020.
6. C. X. Wang et al., *Channel measurements and models for high-speed train communication systems: A survey*, *IEEE Commun. Surv. Tutor.* **18** (2016), no. 2, 974–987.
7. K. Guan et al., *Semi-deterministic path-loss modeling for viaduct and cutting scenarios of high-speed railway*, *IEEE Antennas Wirel. Propag. Lett.* **12** (2013), 789–792.
8. T. Zhou et al., *Channel characterization in high-speed railway station environments at 1.89 GHz*, *Radio Sci.* **50** (2015), 1176–1186.
9. T. Domínguez-Bolaño et al., *Experimental characterization of LTE Wirel. links in high-speed trains*, *Wirel. Commun. Mob. Comput.* **2017** (2017), 1–20.
10. S.-D. Li et al., *Channel measurements and modeling at 6 GHz in the tunnel environments for 5G wireless systems*, *Int. J. Antennas Propag.* **2017** (2017).

<sup>1</sup>During the entire measurements, the maximum speed of the train was 170 km/h; for safety reasons, the train was moving at 130 km/h for the Doppler measurements.

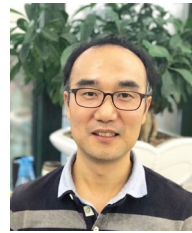
11. X. Wu et al., *28 GHz indoor channel measurements and modeling in laboratory environment using directional antennas*, in Proc. Eur. Conf. Antenna Propag. (EuCAP) (Lisbon, Portugal), Apr. 2015.
12. S. Sun et al., *Propagation path loss models for 5G urban micro- and macro-cellular scenarios*, in Proc. IEEE Veh. Technol. Conf. (VTC Spring), (Nanjing, China), May 2016.
13. J. Lee et al., *Measurement-based propagation channel characteristics for millimeter-wave 5G giga communication systems*, ETRI J. **38** (2016), no. 6, 1031–1041.
14. S. Hur et al., *Proposal on millimeter-wave channel modeling for 5G cellular system*, IEEE J. Sel. Top. Signal Process. **10** (2016), 454–469.
15. D. He et al., *Channel measurement, simulation, and analysis for high-speed railway communications in 5G millimeter-wave band*, IEEE Trans. Intell. Trans. Syst. **19** (2017), 3144–3158.
16. J. Kim et al., *A comprehensive study on mmwave-based mobile hotspot network system for high-speed train communications*, IEEE Trans. Veh. Technol. **68** (2018), 2087–2101.
17. G. Yue et al., *Millimeter-wave system for high-speed train communications between train and trackside: System design and channel measurements*, IEEE Trans. Veh. Technol. **68** (2019), 11746–11761.
18. D. He et al., *Stochastic channel modeling for railway tunnel scenarios at 25 GHz*, ETRI J. **40** (2018), 39–50.
19. K. E. Guan et al., *Towards realistic high-speed train channels at 5G millimeter-wave band—part I: paradigm, significance analysis, and scenario reconstruction*, IEEE Trans. Veh. Technol. **67** (2018), 9112–9128.
20. J. J. Park et al., *Millimeter wave vehicular blockage characteristics based on 28 GHz measurements*, in Proc. Veh. Technol. Conf. (VTC-Fall), (Toronto, Canada), Sept. 2017, pp. 1–5.
21. J. Kivinen et al., *Wideband radio channel measurement system at 2 GHz*, IEEE Trans. Instrum. Meas. **48** (1999), 39–44.
22. M. Schmieder et al., *Measurement and characterization of 28 GHz high-speed train backhaul channels in rural propagation scenarios*, in Proc. Eur. Conf. Antennas Propag. (EuCAP 2018), (London, UK), Apr. 2018, pp. 1–5.
23. L. Liu et al., *Position-based modeling for wireless channel on high-speed railway under a viaduct at 2.35 GHz*, IEEE J. Select. Areas Commun. **30** (2012), 834–845.
24. J. Li et al., *Radio channel measurements and analysis at 2.4/5GHz in subway tunnels*, China Commun. **12** (2015), 36–45.
25. K. Guan et al., *Measurements and analysis of large-scale fading characteristics in curved subway tunnels at 920 MHz, 2400 MHz, and 5705 MHz*, IEEE Trans. Intell. Transport. Syst. **16** (2015), no. 5, 2393–2405.

## AUTHOR BIOGRAPHIES



**Jae-Joon Park** received his BS and MS degrees in control and instrumentation from Chungang University of Seoul, Rep. of Korea in 1997 and 1999, respectively. Since 1999, he has been with the Electronics and Telecommunications Research Institute, Daejeon, Rep. of Korea, where he has worked on the development of smart antennas for the FDD/TDD WCDMA system, the WiBro system for broadband wireless Internet

services, and a wideband wireless channel model for 4G and 5G. He is now a principal researcher, and his current research interests include channel measurements and modeling for millimeter-wave high-speed vehicular wireless communications and future terahertz communication systems.



**Juyul Lee** received his PhD degree in electrical engineering from the University of Minnesota, Twin Cities, USA, in 2010. He was with the Agency for Defense Development (ADD), Rep. of Korea, from 1998 to 2000. Since 2000, he has been with the Electronics and Telecommunications Research Institute (ETRI), Rep. of Korea, where he is currently a principal researcher at the Telecommunications and Media Research Laboratory. His research interests include wireless channel modeling, machine learning, and information theory. He has contributed to ITU-R recommendations and reports in Study Group 3 (Propagation), including millimeter-wave propagation models. He is currently the chairman of the ITU-R Correspondence Group 3K-6, which is responsible for studying the impact of higher frequencies (from 6 GHz to 450 GHz) on propagation models and related characteristics. He is a Senior Member of the IEEE and a Member of KICS.



**Kyung-Won Kim** received his BS degree in electrical engineering from Korea University, Seoul, Rep. of Korea, in 2009, and his PhD degree in computer and radio communications engineering from Korea University in 2015, respectively. Since 2015, he has been with the Electronics and Telecommunications Research Institute (ETRI), Daejeon, Rep. of Korea, where he is currently a senior researcher. His current fields of interest include channel measurement, radio signal processing techniques, channel parameter estimation, and channel modeling.



**Heon-Kook Kwon** received his BS and MS degrees in electronics engineering from the School of Engineering, Chungnam National University, Daejeon, Rep. of Korea, in 1997 and 1999, respectively. Since 2004, he has been with the Electronics and Telecommunications Research Institute, Daejeon, Rep. of Korea, where he is now a principal researcher. He has been working on the development of RF systems for mobile communication. His main research interests are RF system designs for next-generation mobile communications.



**Myung-Don Kim** received his BS and MS degrees in electronics engineering from Dong-A University, Busan, Rep. of Korea, in 1993 and 1995, respectively. Since 1995, he has been with the Electronics and Telecommunications Research Institute, where he is currently a principal researcher and a managing director at the Mobile RF Research Section. Since 2006, he has worked on the development of wideband channel sounder and channel models for microwave and millimeter-wave wireless communications. His research interests include radio propagation, field measurement, channel modeling, and RF technologies for next-generation wireless communications.